Chemical Engineering Science 301 (2025) 120747

Contents lists available at ScienceDirect

Chemical Engineering Science

journal homepage: www.elsevier.com/locate/ces

Enhancing the performance of catalysts in turbulent premixed fuel-lean hydrogen/air combustion

Md Nur Alam Mondal [a], Nader Karimi [a,c], S. David Jackson [b], Manosh C. Paul [a,*]

[a] James Watt School of Engineering, University of Glasgow, Glasgow G12 8QQ, United Kingdom
[b] School of Chemistry, University of Glasgow, Glasgow G12 8QQ, United Kingdom
[c] School of Engineering and Materials Science, Queen Mary University of London, London E14 NS, United Kingdom

ARTICLE INFO

Keywords:
Hydrogen premixed combustion
Turbulent combustion modelling
Catalytic combustion
Ultra-lean combustion
Catalyst coating optimisation

ABSTRACT

Catalytic-aided combustion is a proven technique for burning highly lean and ultra-lean mixtures of hydrogen and air. However, the noble catalyst required for combustion is naturally scarce and therefore expensive. In this study, we focus on a numerical investigation to determine the best way of coating a platinum catalyst inside a catalytic hydrogen reactor. We study various planar and non-planar reactors and find that the reactor with a combination of half and full cylinders is the most effective in H_2 conversion. Compared to an equivalent catalytic planar reactor, the non-planar configuration increases the H_2 conversion by 30.7 %. The results show that enhancing mass and heat convection can significantly increase the H_2 conversion. Furthermore, in a non-planar reactor, surfaces with an enhanced mass and heat transfer can achieve up to 50 % catalyst savings when coated with a catalyst, while still maintaining a conversion rate of 2 kg/s per unit of catalytically-coated surface area.

1. Introduction

Catalytic Stabilised Combustion (CSC) is an effective approach for enhancing the fuel conversion and minimising NOx emissions in a fuel-lean mixture combustion system (Fumey et al., 2018; Schlegel et al., 1996; Smith et al., 2005). This method has been applied in a variety of combustion applications, ranging from a portable micro-scale (Pizza et al., 2009; Pizza et al., 2008; Lu et al., 2022) to a large-scale (Appel et al., 2005; Kuper et al., 1999; Wang et al., 2016) heat and power generation system. However, CSC processes in these systems involve a complex set of reaction mechanisms, that includes both catalytic (heterogeneous) and gas-phase (homogeneous) reactions. In a recent work (Mondal et al., 2023), the essential physico-chemicals behind a CSC process were investigated. It was found that the use of a catalyst initiates the surface catalytic reaction, consuming a portion of fuel and subsequently releasing gas-phase molecules. These molecules then promote the gas-phase reactions and further consume the remaining unburned fuel. However, the gas-phase reaction is largely dependent on the fuel concentration, inflow mass flow rate, preheat temperature, and pressure, as reported in the other articles (Ghermay et al., 2011; Schultze and Mantzaras, 2013; Sui et al., 2018; Ghermay et al., 2010; Sui and Mantzaras, 2016). Importantly, for a very lean mixture at atmospheric pressure, the gas-phase reaction occurs near the combustor wall and becomes dominant at a temperature above 1200 K (Appel et al., 2002). In contrast, the fuel conversion at a temperature below 1200 K occurs entirely through the catalytic route which however strongly depends on the amount of the catalyst-coated surface used in combustor. Nevertheless, the catalytic surface reactions are very fast and mass transport-limited (Mondal et al., 2023; Deutschmann et al., 1996), which limits the fuel conversion.. This requires further research for a fundamental understanding of the catalytic process to enhance the catalyst-substrate interaction.

However, a widespread use of the CSC process also comes with a major challenge due to its high cost and limited availability of catalysts, particularly noble metals. Therefore, extensive research is required to identify the most suitable catalyst that can deliver a high catalytic performance. To enhance the catalytic fuel conversion, several geometric modifications have been proposed, including increasing the surface-to-volume (S/V) ratio of a planar reactor. Zade et al. (Qazi Zade et al., 2012) studied this approach in a planar catalytic reactor with a H_2/Air mixture. They found that the H_2 diffusive flux to the reactor walls and inhibition of the gas-phase reaction increase with the S/V ratio. Similarly, Ghermay et al. (Ghermay et al., 2011) investigated both planar and tubular reactors with the characteristic lengths varying from 0.5 mm to 2.0 mm. Under a turbine-like operating condition with a large confinement (S/V), they showed that the reactor inhibits gas-phase combustion at an atmospheric pressure with a surface temperature of

* Corresponding author.
E-mail address: Manosh.Paul@glasgow.ac.uk (M.C. Paul).

https://doi.org/10.1016/j.ces.2024.120747
Received 3 April 2024; Received in revised form 27 August 2024; Accepted 16 September 2024
Available online 17 September 2024

Nomenclature

d	cylinder diameter (m)
D_m	mass diffusivity (m^2/s)
E	total energy (W)
h	reactor height (m)
h_c	heat transfer coefficient (W/m^2K)
J	diffusion flux (kg/m^2s)
k_c	mass transfer coefficient (m/s)
L	length (m)
$\dot{m}$	mass flowrate (kg/s)
m	total of number of surface species (−)
n	total number of gas species (−)
Nu	Nusselt number (−)
p	pressure (N/m^2)
R	reaction rate (kg/m^3s)
Re	Reynolds number (−)
s	molar production rate (mol/m^2s)
S	Surface area (m^2)
Sh	Sherwood number (−)
T	temperature (K)
X	mole fraction (−)
Y	mass fraction (−)
x	streamwise coordinate (m)
y	transverse coordinate (m)

Greek symbols

ρ	density (kg/m^3)
μ	dynamic viscosity (kg/ms)
φ	equivalence ratio (−)
λ	thermal conductivity (W/mK)
Γ	surface site density (mol/cm^2)
Θ	surface coverage (−)

Subscripts

avg	average
cat	catalyst
g	fluid
in	inlet
s	solid
w	wall

up to 1350 K and a preheat temperature of up to 773 K. This approach improves the reactor catalytic efficiency, thus reducing the catalytic surface length and the amount of catalyst used. In addition to increasing the S/V ratio, wall deformation, such as cavities, obstacles, and waviness, can also improve the catalytic performance. For instance, introducing cavities in the design of a micro-reactor has been shown to enhance mass and heat transfer, resulting in improved catalytic conversion, as reported by Li et al. (Li et al., 2010; Li et al., 2012). They showed that the cavities allow better mixing of the reactants to enhance mass and heat transfer, thus resulting in an improved catalytic conversion.

Similarly, Chababe et al. (Chabane et al., 2020) numerically delineated the effects of both cavities and obstacles with a multi-segment coating. They obtained an optimised configuration using obstacles with segmented catalytic walls, which are capable of high catalytic conversion for flame stabilisation. The obstacle walls were coated; thus, these regimes have an effective high catalytic S/V ratio that favours the catalytic reaction. Both Hunt et al. (Hunt et al., 2021) and Esfandiary et al. (Esfandiary et al., 2023) used surface waviness on the reactor walls considering both continuous and discrete coatings. The function of surface waviness is to interrupt the flow and modify the boundary layer of reactants, which alters the catalytic activity. They optimised the reactor configuration with discrete coating and improved the catalytic performance by up to 400 % and 459 % using platinum and nickel, respectively. Discrete coatings were chosen on the wavy surfaces where the Nusselt and Sherwood numbers were higher. Overall, these modifications improved the catalytic efficiency, reduced the catalytic surface length, and used less catalyst. They achieved this by increasing the S/V ratio, which plays a key role in enhancing mass transfer towards the catalytic surface and improving catalytic reactivity.

Nonetheless, most studies of hydrogen/air catalytic combustion (Appel et al., 2005; Appel et al., 2002; Appel et al., 2004; Mantzaras, 2006; Mantzaras, 2019; Zheng and Mantzaras, 2014; Michelon et al., 2015; Mantzaras et al., 2009; Mantzaras, 2014), either experimental or numerical, are limited to the reactors of planar configurations. As discussed earlier, a detailed understanding of the underlying physics inside a reactor with surface deformations is a key path towards improving the performance of catalytic hydrogen/air combustion as well as optimising the use of catalyst. Again, the size of a catalytic planar reactor is crucial for achieving complete combustion of a lean hydrogen/air mixture. Also, from an economic standpoint, an excessive use of catalyst with the catalytic reactor length longer than required is not useful. So, compactness in the design of a catalytic reactor is required for the optimum use of the catalyst for hydrogen conversion. Moreover, the catalytic reacting flow in such cases becomes complex due to the turbulence generated by the flow. Therefore, this requires a thorough understanding of the catalytic process, which is equally important for both planar and non-planar reactor configurations, before finding any potential improvements in CSC systems. For that purpose, a numerical simulation is a convenient and useful approach prior to an experimental investigation. Consequently, this study is focused on the numerical investigation of turbulent catalytic combustion of a premixed lean H_2/air mixture in the proposed configurations (planar and non-planar) to optimise the use of the catalyst for a compact reactor design. These configurations have been chosen with the practical use of a honeycomb burner in mind, where the heat transfer in solid materials can have a significant impact on the catalytic performance (Sui and Mantzaras, 2016; Sui et al., 2016). As a result, heat transfer in solid walls has been included in all configurations. Particular objectives are to provide a better understanding of the catalytic combustion process in the different configurations proposed, which leads to the investigation of catalyst optimisation.

This article is structured in the following manner: Section 2 presents the numerical methodology and validated results. Next, in Section 3.1, the effect of the S/V ratio among the different configurations is discussed. The best possible configurations are compared as a function of the catalytic conversion rate and Nusselt and Sherwood numbers in Section 3.2. Finally, conclusions are made in Section 4.

2. Modelling of turbulent catalytic reacting flow

In our previous study (Mondal et al., 2023), we used a fuel-lean premixed H_2/air mixture at an equivalence ratio of $0.10 \leq \varphi \leq 0.20$ under laminar flow conditions. This mixture was chosen because of its suitability for a low-temperature heating application. Hence, a value of $\varphi = 0.15$ is selected in this work, which is within the studied fuel-lean equivalence ratio limit. Again, the inflow Reynolds number for laminar flow was considered up to 2666 based on the hydraulic diameter ($2\,h$) (Mondal et al., 2023). Therefore, to investigate the catalytic effect at a high Reynolds number in a turbulent regime, we have taken an inflow Reynold number $\geq$ 4200 for a planar reactor. For the reactor configurations with a confined cylinder, the Reynolds number is kept above 3385 (≈846 based on cylinder diameter). However, in both

reactor configurations, the Reynolds numbers considered are above the critical Reynolds number: 3500 ~ 4000 for the planar channel (Forrest et al., 2016), and 150 ~ 225 (based on cylinder diameter) for the channel with cylinder (Forrest et al., 2016; Abe et al., 1995), which justifies the turbulent assumption in this study. Numerical computations are carried out with a RANS code that includes a species transport model and a detailed description of heterogeneous (surface) and homogenous (gas phase) kinetics. The surface mechanism of Deutschmann et al. (Deutschmann et al., 1996) is used for modelling the catalytic reactions as it has been extensively validated against the experiments. For the gas phase reactions, five well-known mechanisms were tested and compared with measurements to find a suitable mechanism for predictions of the combined effect of the couple chemistry in the catalytic process. The governing equations and numerical settings to simulate the turbulent catalytic reacting flow are provided below.

2.1. Governing equations

Reynolds-Averaged Navier Stokes (RANS) computations with detailed chemistry (both homogeneous and heterogeneous) are performed to simulate turbulent reacting flow in a catalytic reactor with inner surfaces coated with Pt. The Navier-Stokes, species transport, and energy equations are solved considering Newtonian, incompressible, steady-state, and multicomponent flow assumptions. The equations are stated with the tensor notation as follows:

$$Continuity: \frac{\partial}{\partial x_i}(\rho U_i) = 0 \tag{1}$$

where ρ is the density, $u = U + u'$is the instantaneous velocity. U and u' are the mean and fluctuation components, respectively.

$$Momentum: \frac{\partial}{\partial x_j}(\rho U_i U_j) = -\frac{\partial P}{\partial x_i} + \frac{\partial}{\partial x_j}\left[\tau_{ij} - \rho\overline{u_i' u_j'}\right] \tag{2}$$

where $\rho\overline{u_i' u_j'}$ is the Reynolds stresses and τ_{ij} is the viscous (or deviatoric) stress tensor,

$$\tau_{ij} = \mu\left(\frac{\partial U_i}{\partial x_j} + \frac{\partial U_j}{\partial x_i} - \frac{2}{3}\delta_{ij}\frac{\partial U_k}{\partial x_k}\right) \tag{3}$$

To model the Reynolds stresses, the low Reynolds (LR) variant of k-ε turbulence models proposed by Abe et al. (Abe et al., 1995) is chosen. This choice is due to the intense heating from the hot catalytic wall, which laminarises the turbulent flow to a certain extent, necessitating an overdissipative model compared to the standard k-ε model (Appel et al., 2005). The overdissipation of turbulence is accomplished via the functions f_μ and f_2 in Equations (7) and (8). The LR model was validated for catalytic turbulent reacting flow (Appel et al., 2005), is therefore employed in this study. The equations used for the LR model are given below:

Turbulent kinetic energy (k):

$$\frac{\partial}{\partial x_j}(\rho U_j k) = \frac{\partial}{\partial x_j}\left[\left(\mu + \frac{\mu_t}{\sigma_k}\right)\frac{\partial k}{\partial x_j}\right] - \rho\overline{u_i' u_j'}\frac{\partial U_i}{\partial x_j} - \rho\varepsilon \tag{4}$$

Dissipation rate of k (ε):

$$\frac{\partial}{\partial x_j}(\rho U_j \varepsilon) = \frac{\partial}{\partial x_j}\left[\left(\mu + \frac{\mu_t}{\sigma_\varepsilon}\right)\frac{\partial \varepsilon}{\partial x_j}\right] - \rho C_{\varepsilon 1}\frac{\varepsilon}{k}\overline{u_i' u_j'}\frac{\partial U_i}{\partial x_j} - \rho C_{\varepsilon 2} f_2 \frac{\varepsilon}{k}\varepsilon, \tag{5}$$

where

$$-\rho\overline{u_i' u_j'} = \mu_t\left(\frac{\partial U_i}{\partial x_j} + \frac{\partial U_j}{\partial x_i}\right) - \frac{2}{3}\rho k\delta_{ij} \; and \; \mu_t = \rho C_\mu f_\mu \frac{k^2}{\varepsilon} \tag{6}$$

In equations (4)-(6), the model functions and constants are taken as the same as in the study of Abe et al. (Abe et al., 1995): $\sigma_k = 1.4$, σ_ε=1.4, $C_{\varepsilon 1} = 1.5$, $C_{\varepsilon 2} = 1.9$, $C_\mu = 0.09$,

$$f_\mu = \left[1 - \exp\left(-\frac{y^*}{14}\right)\right]\left[1 + \left(1 + \frac{5}{R_t^{3/4}}\exp\left\{-\left(\frac{R_t}{200}\right)^2\right\}\right)\right] \; and \tag{7}$$

$$f_2 = \left[1 - 0.3\exp\left\{-\left(\frac{R_t}{6.5}\right)^2\right\}\right]\left[1 - \exp\left(-\frac{y^*}{3.1}\right)\right]^2, \tag{8}$$

where $y^* = u_\varepsilon y/\upsilon$, $R_t = k^2/\upsilon\varepsilon$ and $u_\varepsilon = (\upsilon\varepsilon)^{1/4}$ is the Kolmogorov velocity scale. The purpose of both the functions f_μ and f_2 is to make the model overdissipative compared to the standard high Reynolds number model, with both the functions approaching unity far from the wall (Appel et al., 2005).

Energy:

$$\frac{\partial}{\partial x_i}(u_i(\rho E + p)) = \frac{\partial}{\partial x_i}\left[\left(\lambda + \frac{c_p\mu_t}{Pr_t}\right)\frac{\partial T}{\partial x_i} - \sum_{j=1}^{n} h_{g,j}J_{g,j} + \tau_{ij}u_i\right] + S_h, \tag{9}$$

where E, T, λ, h, J and S_h denote the total energy, temperature, effective conductivity, enthalpy, diffusion flux of species j, and sources of energy due to chemical reaction, respectively. Pr_t is the turbulent Prandtl number, and its value is set to 0.85.

$$Species\ transport: \frac{\partial}{\partial x_i}(\rho u_i Y_{g,j}) = \frac{\mu_t}{Sc_t}\frac{\partial Y_{g,j}}{\partial x_i} - \frac{\partial J_{g,j}}{\partial x_i} + R_{g,j} \tag{10}$$

$$where\ J_{g,j} = -\rho D_{m,j}\frac{\partial Y_{g,j}}{\partial x_i} - \frac{D_{T,j}}{T}\frac{\partial T}{\partial x_i} \tag{11}$$

Here, Sc_t is the turbulent Schmidt number, and its value is set to 0.85. R denotes the rate of production and destruction of gas species. D_m and D_T are the mass diffusion and the thermal diffusivity of gas species, respectively. To compute the diffusion fluxes, J, Maxwell-Stefan and Fick's law diffusion coefficients (Stewart, 1995), including the thermal diffusion (Merk, 1959) for light species are adopted.

Surface species coverage:

$$\frac{d\theta_j}{dt} = \frac{s_j}{\Gamma} = 0 (j = 1, 2..., m), \tag{12}$$

where θ is the surface species coverage, s is the surface species molar production rate and Γ is the surface site density. The transient term vanishes at steady state, and the net production rate becomes zero.

To model heat transfer in solid, the heat conduction equation is as follows:

$$\frac{\partial}{\partial x_i}\left(\lambda_s\frac{\partial T_s}{\partial x_i}\right) = 0, \tag{13}$$

where λ_s and T_s are the solid conductivity and temperature, respectively.

2.2. Boundary conditions

As shown in Fig. 1, the catalytic reactor is defined in a two-dimensional Cartesian frame. It brings in premixed reactants of hydrogen and air through the inlet, initiates the reaction on the catalytic surfaces, and then releases the resulting products through the outlet. The inflow conditions are kept uniform in terms of the flow velocity, temperature, and species mass fraction, with an inflow turbulence intensity of 5 % (estimated based on the flow Reynolds number). At the outlet, all the variables experience a zero-gradient condition, except for the pressure, which is maintained at an atmospheric level. The gas–solid boundary conditions at the interface of the catalytic reactor are as follows:

- The flow velocity components, $u = 0$, and $v = 0$, in the x and y directions, respectively, as the no-slip conditions.
- For the turbulence parameter, $\varepsilon_s = 2\upsilon\left(\partial\sqrt{k}/\partial y\right)^2$ is employed.

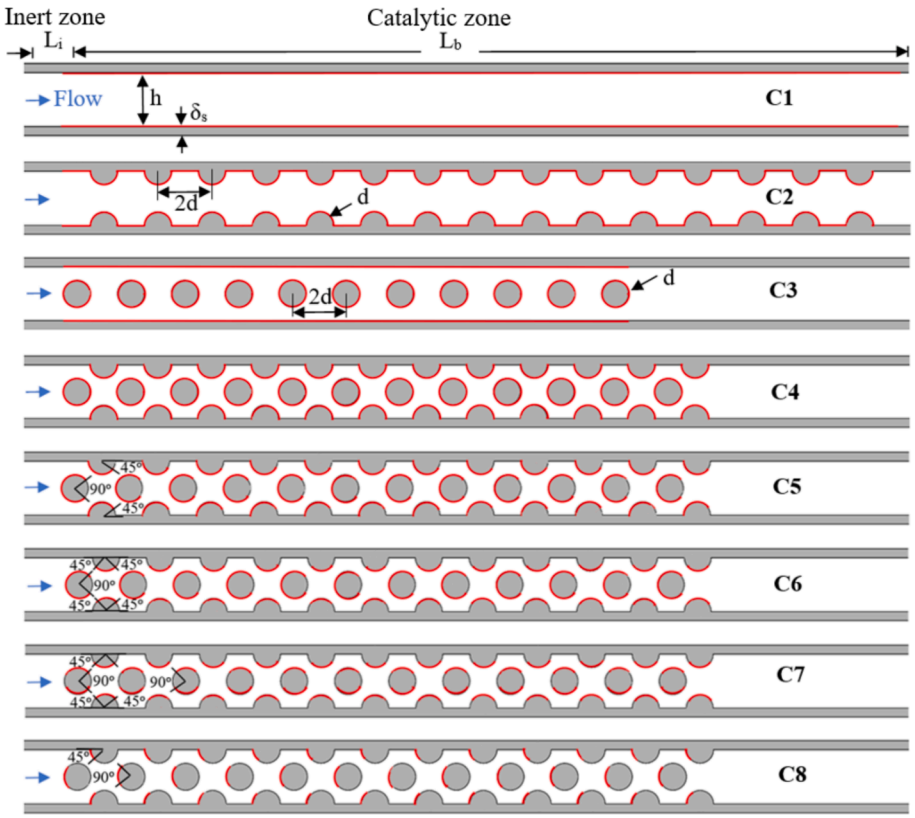

Fig. 1. Schematics of the various catalytic reactors. The red colour denotes the catalytic surface in the catalytic zone. (For interpretation of the references to colour in this figure legend, the reader is referred to the web version of this article.)

- The gas phase species boundary conditions at the gas–solid interface are specified by $[\rho D_m(\partial Y_g/\partial y)]_w = W_g s_g$, where W_g and s_g represent the molecular weight and catalytic molar production rate of gas species. Here, the mean catalytic reaction rates are evaluated at the mean wall temperature and the corresponding mean concentration of gas species, and they are basically treated using a "laminar-like" closure as discussed in referenced work (Appel et al., 2005).
- The thermal boundary conditions at the interface are set coupled.
- The outer walls, including the vertical facets of the plates, are considered adiabatic.
- The thermal conductivity of $\lambda_s = 16.27\ \mathrm{Wm^{-1}K^{-1}}$ is used to account for heat conduction in solids.
- As the outer walls are adiabatic, the radiation of the hot catalytic surfaces towards the inlet and outlet is simulated using the discrete ordinates (DO) model. The DO model is uncoupled, and a value of 10 is set for the energy iterations per radiation iteration.
- The radiation heat transfer is considered at the boundary temperature at the inlet and outlet enclosures with an internal emissivity of 1.0.

2.3. Solutions algorithm and solver setting

Computations are performed on eight configurations (C1-C8), as shown in Fig. 1 with the design parameters listed in Table 1. The L_i and L_b in reactor configuration denote the length of the inert zone and the catalytic zone, respectively. The configuration C1 is a planar reactor, which consists of two parallel plates with a thickness (δ_s) of 0.5 mm placed at a distance h, where the inner surfaces are Pt-coated. In the previous studies (Qazi Zade et al., 2012; Ghermay et al., 2011), it was found that the gap between the plates has a significant impact on the mass and heat transfer rates as well as on the catalytic process. To investigate this effect, we vary the value of h to 1-, 2-, 3-, 5-, and 7-mm. Again, a similar planar configuration C1 of h = 3.5-mm is chosen to serve as a reference for comparisons with modifications considered for catalyst optimisation.

Table 1
Computational conditions.

Catalytic reactor	h (mm)	L_i (mm)	L_b (mm)	S_{cat} (mm^2)	Re	Residence time (s)
C1	1	0	350	700	4200	0.010586
	2	0	500	1000	4200	0.030248
	3	0	700	1400	4200	0.063520
	5	0	900	1800	4200	0.136116
	7	0	1100	2200	4200	0.232909
	3.5	5.25	75	115	4353	0.006927
C2	3	5.25	75	115.69	3680	0.006927
C3	3	5.25	75	114.84	3811	0.006927
C4	3	5.25	75	113.1	3385	0.006927
C5	3	5.25	75	84.82	3385	0.006927
C6	3	5.25	75	70.69	3385	0.006927
C7	3	5.25	75	56.55	3385	0.006927
C8	3	5.25	75	28.27	3385	0.006927

Configuration C2 features half cylinders (HC) of diameter d = 1.5-mm, symmetrically placed on the inner surfaces of the planar reactor with a distance d between them. The catalytic surfaces consist of 15 circular surfaces of HCs and 15 flat surfaces (P). C3 includes full cylinders (FC) of diameter d at the mid-plane of the reactor with a distance d between them, and the circular surfaces of 11 FCs and both the upper and lower inner surfaces of the planar reactor are defined as the catalytic surfaces. However, C4 is a combination of HC and FC placed alternately inside the reactor. The HCs are attached to the upper and lower inner surfaces and symmetrically placed. The FCs are placed in the mid-plane of the reactor. Here, the circular surfaces of 12 HCs and 12 FCs are the catalytic surfaces. However, the number of HCs and FCs for C2, C3, and C4 is considered to keep approximately the same amount of catalyst

surface as C1. The C5, C6, C7, and C8 configurations are the same as C4 but with a reduction of 25 %, 37.5 %, 50 %, and 75 % catalyst from C4, respectively. The catalytic surface for these configurations is selected on specific locations of the circular surfaces where heat and mass transfer are effective.

A Finite Volume Method (FVM) is used to solve the governing equations for turbulent flow variables. Ansys Fluent 2023 R2 version was used for computations, with a 2-D steady-state planar and pressure-based solver. The LR variant of the k-ε model was set as the viscous model, and the species transport model was used to solve the volumetric and wall surface reactions. The chemistry solver was stiff, and the integration method was ISAT. The reaction rates were computed using Eddy-dissipation-concept (EDC). The SIMPLE scheme was used for pressure velocity coupling. For spatial discretisation, least square cell-based, and second-order method were set for gradients and pressure, respectively. A second-order upwind method was used for all other variables. The solution convergence criteria of 10^{-6} were set for all the residuals.

2.4. Chemical kinetics

To model the process of hydrogen catalytic combustion, we used both gas-phase and surface detailed reaction mechanisms. Our focus was on finding the appropriate gas-phase mechanism that could accurately predict the location of the flame, as the ignition process is complex and subject to debate. We investigated five different gas-phase mechanisms by Warnatz (Warnatz et al., 1994), Marinov (Marinov et al., 1995), Li (Li et al., 2004), kim (Kim et al., 1994) and Fureby (Vincent-Randonnier et al., 2019). For the surface mechanism, we employed the model developed by Deutschmann et al. (Deutschmann et al., 1996), which simulates H_2 oxidation over Pt through three reversible and eleven irreversible reactions involving five surface and six gas-phase species. The gas-phase and surface reaction rates were evaluated using CHEMKIN (Kee et al., 1989) and Surface-CHEMKIN (Coltrin et al., 1996), respectively and transport properties were calculated using CHEMKIN transport database (Kee et al., 1986). However, the mass-weighted mixing law was used to compute the mixture gas viscosity and thermal conductivity. For mass diffusivity and thermal diffusion coefficient, we utilised the kinetic theory. Overall, our approach enabled us to accurately model hydrogen catalytic combustion.

2.5. Mesh resolutions

The computational domain for C1 with varying h is considered comparatively long to ensure complete combustion. For $h = 7$ mm, a structured grid of 1500 × 150 points (in the x- and y-directions, respectively) is used for the fluid domain, with refinement towards the inlet and walls. The solid domain is discretised with the 1500 × 30 grid points (in the x- and y- directions, respectively). A similar grid resolution is used for the other configurations as grid requirements for $h < 7$ mm are less strict. For configurations C2, C3, and C4, a separate grid resolution test is conducted due to their distinct design conditions. All the configurations have several irregular surfaces with high gradients of flow variables, requiring grid refinement near the walls and irregular surfaces. For comparison, three grid sizes of each configuration are taken and denoted as M1, M2, and M3 (Table 2). For C2 in Fig. 2 (a), the variation of catalytic temperatures along the reactor length and transverse mean H_2 distribution (at x = 7.5 mm and 9 mm) are compared and it shows no significant changes among the tested grid sizes. Similarly, for C3 and C4, the grid test is performed using the centreline temperatures along the reactor length and transverse mean H_2 profiles (at $x = 7.5$ mm and 9 mm) shown in Fig. 2(b) and (c), respectively. However, based on the comparisons shown and the precision requirement, the grid size M2 for the respective configuration is chosen for the computations.

Table 2
Number of grids tested.

Type	C2		C3		C4	
	Fluid	Solid	Fluid	Solid	Fluid	Solid
M1	120,305	62,376	150,460	79,845	124,307	85,998
M2	176,625	120,874	198,625	121,878	175,627	121,878
M3	236,705	148,786	262,020	144,685	234,147	162,558

2.6. Validation of the numerical solutions

The steady-state solutions obtained from the numerical calculations were validated by comparing them with the experimental results of Appel et al. (Appel et al., 2005). The same reactor configuration was adopted as that used in the experiment. The operating parameters were replicated, and the measured wall temperatures were treated as the wall boundary conditions. The validated results presented in Fig. 3 show the mean values of the species (H_2 and H_2O) and temperatures at the various axial locations. The results compare five gas-phase mechanisms with the experimental dataset. The objective here is to attain a suitable mechanism for the prediction of a realistic catalytic process. At $x = 25$-mm, all the mechanisms accurately capture the X_{H2} and are in good agreement with the measurements. However, they underpredict the X_{H2} far from the walls near the reactor centre region with increasing x. Overall, the predictions of Warnatz (Warnatz et al., 1994), Kim (Kim et al., 1994), and Li (Li et al., 2004) are similar, with Marinov (Marinov et al., 1995) and Fureby (Vincent-Randonnier et al., 2019) showing higher underprediction far downstream. Warnatz (Warnatz et al., 1994), Kim (Kim et al., 1994), and Li (Li et al., 2004) produced similar predictions of H_2O and T, but they underpredict near the walls with increasing x. Compared to them, Marinov (Marinov et al., 1995) and Fureby (Vincent-Randonnier et al., 2019) have less underpredictions near the walls. To better justify the mechanisms, the OH contour plots in Fig. 4 are presented along with the numerical and experimental results of Appel et al. (Appel et al., 2005). The onset of gas-phase ignition (indicated by the vertical downward arrow) and OH ppmv level are taken into consideration for comparisons. The results indicate that an early ignition occurs with almost all the mechanisms including the numerical results of Appel et al. By comparison, the ignition locations of Warnatz (Warnatz et al., 1994) and Kim (Kim et al., 1994), are nearly similar and closer to measurement.

However, the underpredictions obtained are approximately 21.7 %, 23.5 %, 40.1 %, 61.7 %, and 66.8 % for Warnatz (Warnatz et al., 1994), Kim (Kim et al., 1994), Li (Li et al., 2004), Marinov (Marinov et al., 1995) and Fureby (Vincent-Randonnier et al., 2019), respectively. Similarly, the percentage variations of maximum OH ppmv among these mechanisms are 3.33 %, 62.08 %, 42.5 %, 139.58 %, and 107.08 %, respectively. Overall, the Warnatz (Warnatz et al., 1994) mechanism provides reasonable agreement with the experimental measurements and is therefore chosen for the present study.

3. Results and discussion

Firstly, we present the results of the combustion of fuel-lean premixed H_2/air in a catalytic planar reactor with varying h (i.e., the gap between the walls). The aim is to provide an in-depth understanding of catalyst reduction and to facilitate the discussion of reactor development with an optimum use of catalysts under similar operating conditions. Next, we discuss the distribution of the Nusselt and Sherwood numbers on catalytic surfaces across different configurations, followed by a comparison of H_2 consumption rates.

3.1. Planar reactor configurations

Fig. 5 shows the predicted H_2 conversion for each h. We define H_2 conversion as follows:

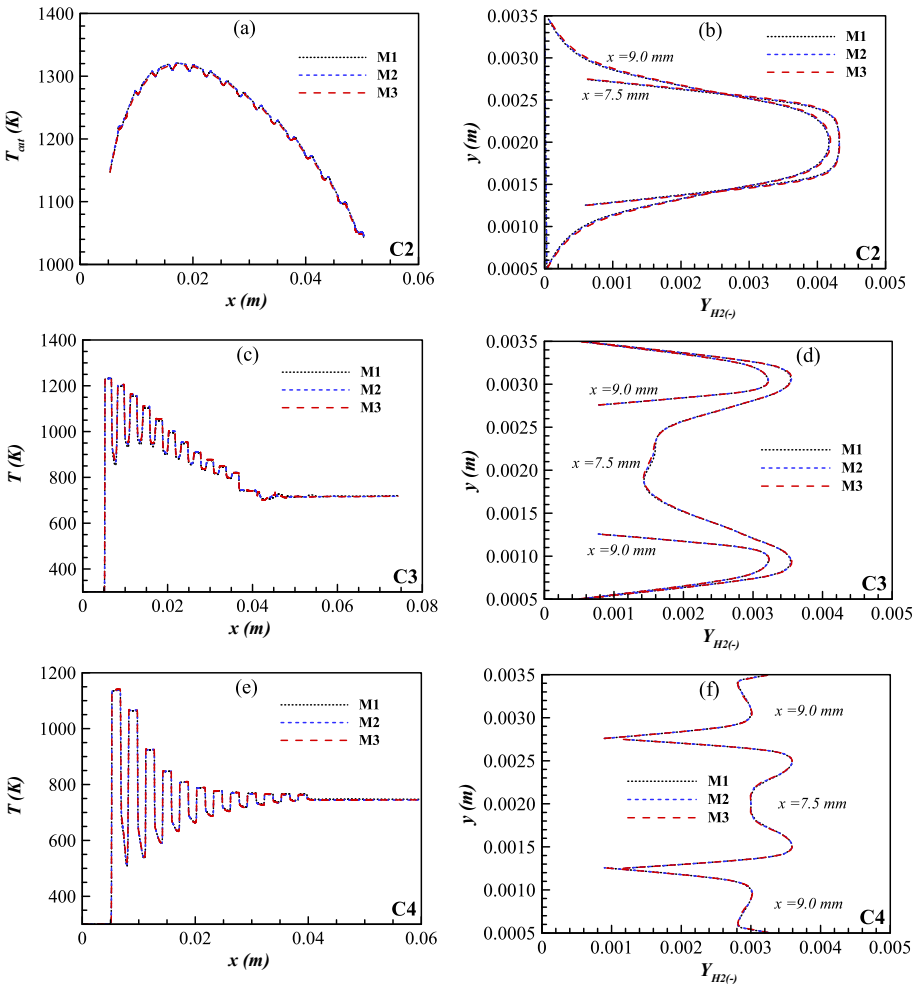

Fig. 2. Effect of grid resolution for the configurations of C2, C3 and C4, (a) temperature on catalytic surface, T_{cat} (c, e) midplane temperature inside the reactor, T (b, d, f) transverse profile of H_2 mass fraction at location x = 7.5 mm and 9 mm.

$$H_2\ conversion(\%) = \frac{Y_{H2,avg,in} - Y_{H2,avg,x}}{Y_{H2,avg,in}} \times 100 \quad (14)$$

where $Y_{H2,avg,in}$ and $Y_{H2,avg,x}$ are the average H_2 mass fraction at the inlet and axial positions, respectively. In Fig. 5(a), the H_2 conversion reaches nearly 99.9 % across the entire length of the catalytic reactor for various reactor heights (h). The results indicate that as the reactor height (h) decreases, a shorter catalytic reactor length is required to achieve complete H_2 conversion. This is due to the intensified diffusion of H_2 species with decreasing h, as discussed in Fig. 5(b). The figure illustrates the transverse distributions of H_2 and H_2O at x = 10-mm for all the planar configurations. As h decreases, Y_{H2} decreases because of the strong diffusion of H_2 towards the reactor walls. This enhanced diffusion leads to greater H_2 consumption in the catalytic process, resulting in increased H_2O production at lower h.

The catalytic wall temperature (T_w) along the reactor length for different reactor heights (h) are shown in Fig. 5(a). The peak T_w values are located close to the upstream and shifts along the reactor length with increasing h. It is observed that a significant length of catalytic surface reaches superadiabatic temperatures, a common occurrence in H_2 catalytic combustion under nearly adiabatic conditions. Operating a reactor under such conditions is considered unfavourable, as discussed in literature (Appel et al., 2005; Appel et al., 2002). The variation in T_w along the reactor length is a result of heat transfer from hot surface to incoming mixtures, as well as heat conduction in solid. The H_2 conversions in Fig. 5(a) for different reactor heights are obtained by keeping the same inflow conditions. However, the contributions of the gaseous reaction and the catalytic reaction pathways H_2 to conversion vary with the reactor heights (h), as shown in Table 3.

For the reactor of h = 1 mm, the combustion mode is entirely catalytic. As h increases, the contribution of gaseous combustion also rises. In order to assess the effect of gaseous combustion at different reactor heights, some calculations are performed while maintaining constant operating conditions, but without gas-phase chemistry.

Fig. 6 illustrates the changes in surface coverages of H(s), O(s), and OH(s) on the catalytic surface. For convenience, pure catalytic chemistry and coupled chemistry are referred as PC and CC, respectively. The surface coverage of H(s) and O(s) are controlled by the adsorption rate and near wall concentrations of H_2 and O_2, respectively. Again, under fuel lean condition, the O(s) is the main coverage, and is strongly dependent on wall temperature. At high temperatures, as shown in Fig. 6 (b), the O(s) is low, which promotes H_2 adsorption. As temperature decreases, the O(s) increases while H(s) in Fig. 6(a) decreases due to lower concentrations of H_2.

The effect of gas-phase chemistry becomes more significant as reactor height (h) increases. For h = 1-mm, there is no variation between CC and PC, indicating purely catalytic combustion. At a higher reactor height of h = 3-mm, a variation in H(s) is observed at peak values within a very limited catalytic length, along with changes in O(s) and OH(s). This suggests that gas-phase chemistry has a small contribution on the catalytic process at this height. However, for h = 5 mm and 7 mm, the effect of gas-phase chemistry becomes more substantial over a broader catalytic length. The flame inside the reactor is attached to the catalytic wall, which prevents the H_2 adsorption, resulting in lower H(s) in CC

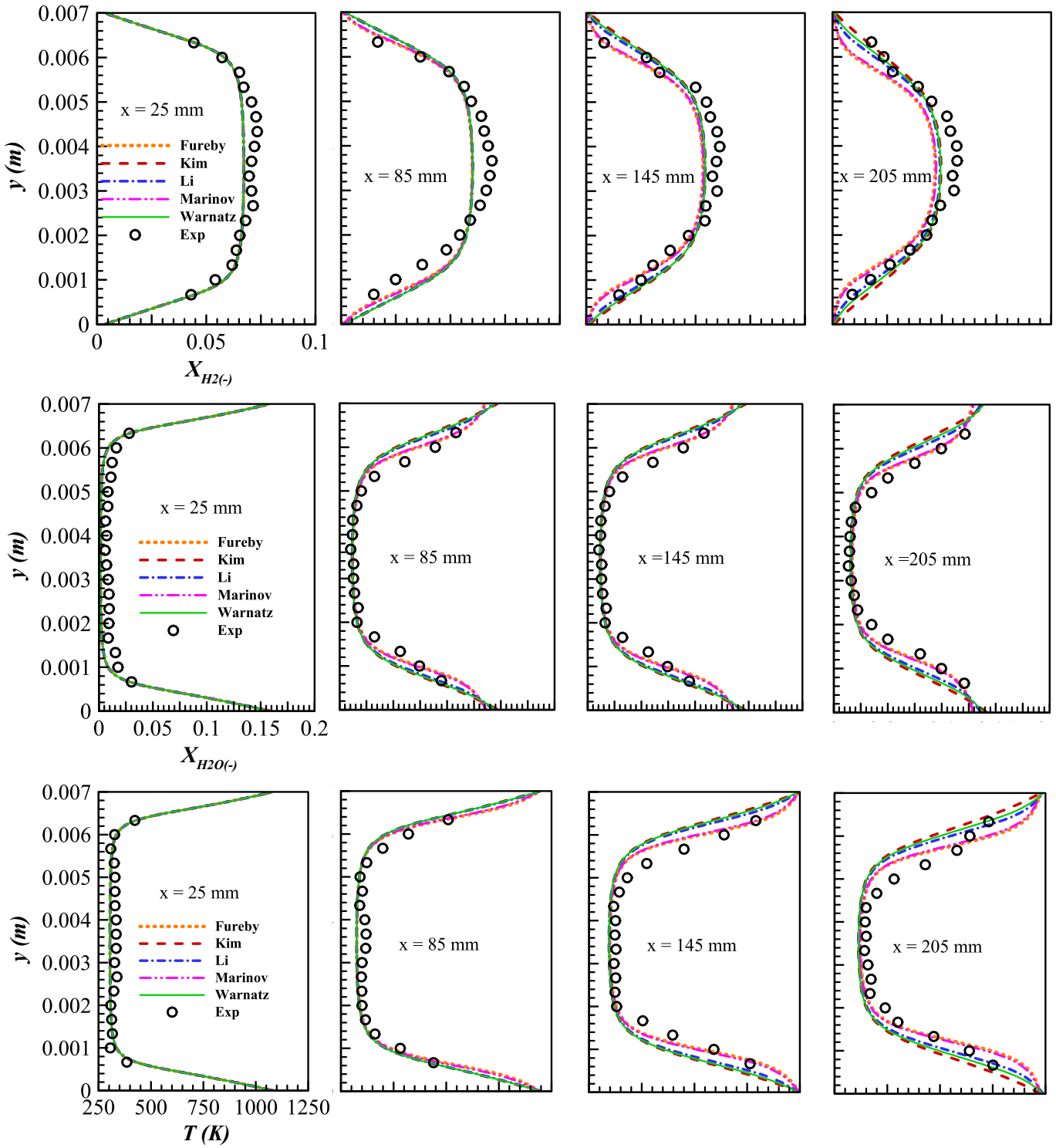

Fig. 3. Comparisons of species and temperature mean profiles at different axial positions at $\varphi = 0.18$, $T_{in} = 300$ K, $Re = 15390$.

within the flame regime. Within the reactor, the flame is attached to the catalytic wall, which hinders H_2 adsorption, leading to lower H(s) in CC within the flame region. Conversely, excess O_2 promotes O_2 adsorption in the flame region, increasing O(s) coverage. Similarly, OH adsorption rises because the catalyst acts as a sink for homogeneously produced OH, as discussed in earlier studies (Mondal et al., 2023). Beyond the flame region, the reaction shifts entirely to the catalytic mode.

3.2. Conceptual design modifications for optimal catalyst

3.2.1. Combustion characteristics

Computations on the modified reactors are now being carried out using the same numerical approach as the planar reactor. Fig. 7 presents the contours of the species mass fraction such as H_2, H_2O, and OH, as well as the flame temperatures for configurations C1, C2, C3, and C4. The computation maintains almost the same residence time and the same catalyst surface area for these reactors to establish a clear

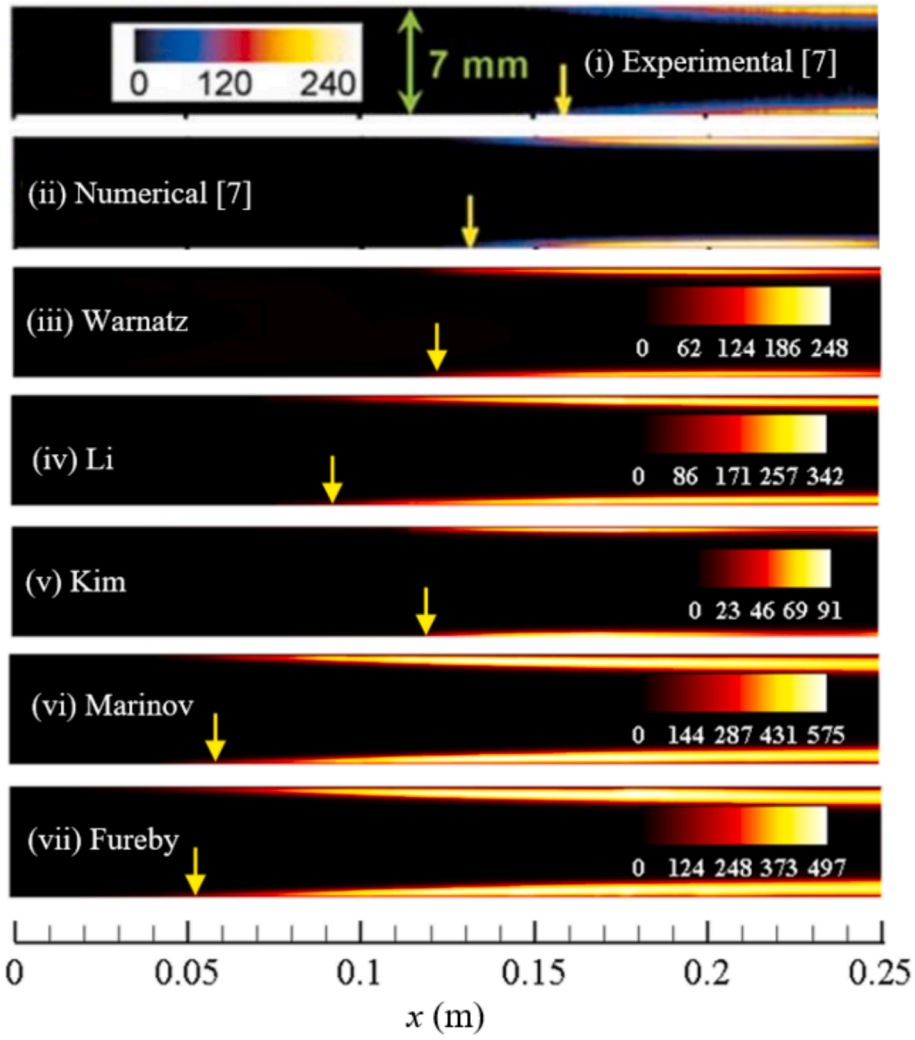

Fig. 4. OH contour (ppmv) (arrow indicates the onset of gas-phase ignition) at $\varphi = 0.18$, $T_{in} = 300$ K and $Re = 15390$.

understanding of how each configuration affects the catalytic process. The planar reactor C1 of $h = 3.5$-mm is used as a reference for comparisons.

Compared to C1, it is observed from the Y_{OH} contour in Fig. 7(c) that the gas-phase chemistry plays a strong role, where the flames are ignited and stabilised near the inlet on the non-catalytic walls. The flames are also evident in the locations between the two half cylinders (HC). As a result, the Y_{H2} consumption and Y_{H2O} production in the flame regime is high, as also shown in Fig. 7(a) and Fig. 7(b), respectively. Additionally, the T contour in Fig. 7(d) indicates that the temperature increases in the solid domain due to a combination of gas-phase and catalytic combustion, which leaves the reactor core at a low temperature. However. The thickness of the solid plays a crucial role in catalytic reacting flows, particularly when subjected to temperature fluctuations, as highlighted in the work by Arani et al. (Arani et al., 2019). As discussed in their article, a wall thickness of 50 μm allows the solid to closely track the temperature fluctuations imposed by the reacting flow. In the current modelling, however, we employ a significantly thicker wall of 0.5 mm (500 μm). This increased thickness enhances the solid's thermal inertia, thereby limiting the potential for fluctuations in the wall temperature.

Fig. 7(c) shows that the flames of C3 are ignited on the non-catalytic walls but are not as strong as C2. In the catalytic regime, no significant Y_{OH} is observed, indicating that the combustion mode is purely catalytic. Comparatively, the significant Y_{H2} consumption is observed in the flame regime, specifically on the catalytic flat surfaces between the two full cylinders (FC), as shown in Fig. 7(a). Consequently, the Y_{H2O} production is higher in those locations, as depicted in Fig. 7(b). In addition, the T contour in Fig. 7(d) shows that the catalytic process influences the temperature distributions in solid, thus high temperatures in the solid regime are observed in both the flat and cylinder domains up to $x = 7d$, then gradually decrease with x as a low H_2 concentration for the catalytic process. When comparing the Y_{OH} of C4 to that of the other configurations in Fig. 7(c), the Y_{OH} contribution is insignificant over the domain. This means that no gas-phase ignition is observed in this case, and the mode of combustion is purely catalytic. Therefore, the Y_{H2} consumption takes place on the catalytic surfaces shown in Fig. 7(a), and the Y_{H2O} production in Fig. 7(b) is higher near the regime of catalytic surfaces. Regarding the temperature (T) in Fig. 7(d), it is almost uniform in the solid domain except in the first two full cylinders where the temperature is comparatively high. However, the orientation of HCs, FCs or both combinations inside the reactor has a significant effect on the flow field and influenced the heat and mass exchange between the flow and catalytic surfaces. Fig. 8 displays the flow patterns along the length of the catalytic reactor. The reactor length is presented here only from $x = 0.25$-mm to $x = 25.5$-mm. For C2, the flow gets separated downstream of HC and vortices are formed. The vortices are located between two HCs and attached to both the upper and lower walls which are almost symmetrical about the mid plane. Similarly, the flow separation for C3 occurs downstream of FC, and the region between two FCs is covered by the vortices. For C3, the vortices are formed downstream of

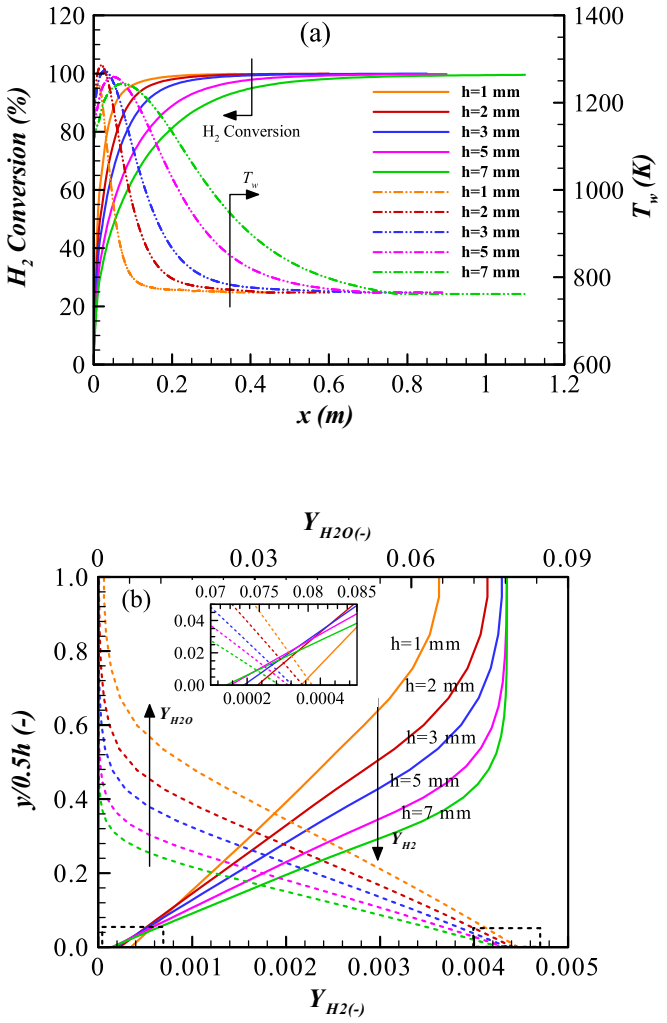

Fig. 5. Planar catalytic reactor: (a) left axis: H_2 Conversion; right axis: temperature distribution on catalytic wall (T_w) (b) H_2 and H_2O distribution at x = 10 mm, φ = 0.15, T_{in} = 300 K, Re = 4200.

Table 3
Gaseous and catalytic conversion rates at different planar reactor heights.

Planar reactor (C1)	$h = 1$ mm	$h = 2$ mm	$h = 3$ mm	$h = 5$ mm	$h = 7$ mm
$\dot{m}_{H2}$ inlet ($\times 10^4$ kg/s)	1.63921	1.63921	1.63921	1.63921	1.63921
Gas. conv. ($\times 10^4$ kg/s)	0.00249	0.02899	0.10915	0.19817	0.23327
Cat. conv. ($\times 10^4$ kg/s)	1.63672	1.61022	1.53006	1.44104	1.40594
Gas. conv. (%)	0.15	1.77	6.66	12.09	14.23
Cat. conv. (%)	99.85	98.23	93.34	87.91	85.77

HCs and FCs, but the vortices size are comparative smaller than that of C2 and C3. Again, the branch of vortices near upstream of HCs is smaller in size than the vortices near downstream of HCs. Furthermore, there is no vortices observed at the upstream of FCs. After all, the vortices have significant effect on the heat transfer, and mass transfer of fuel, thus influencing the catalytic combustion process.

3.2.2. Heat and mass transfer

To assess the heat and mass exchange between the flow and catalytic surfaces, the Nusselt (*Nu*) and Sherwood number (*Sh*) are considered, and their definition are given as follows:

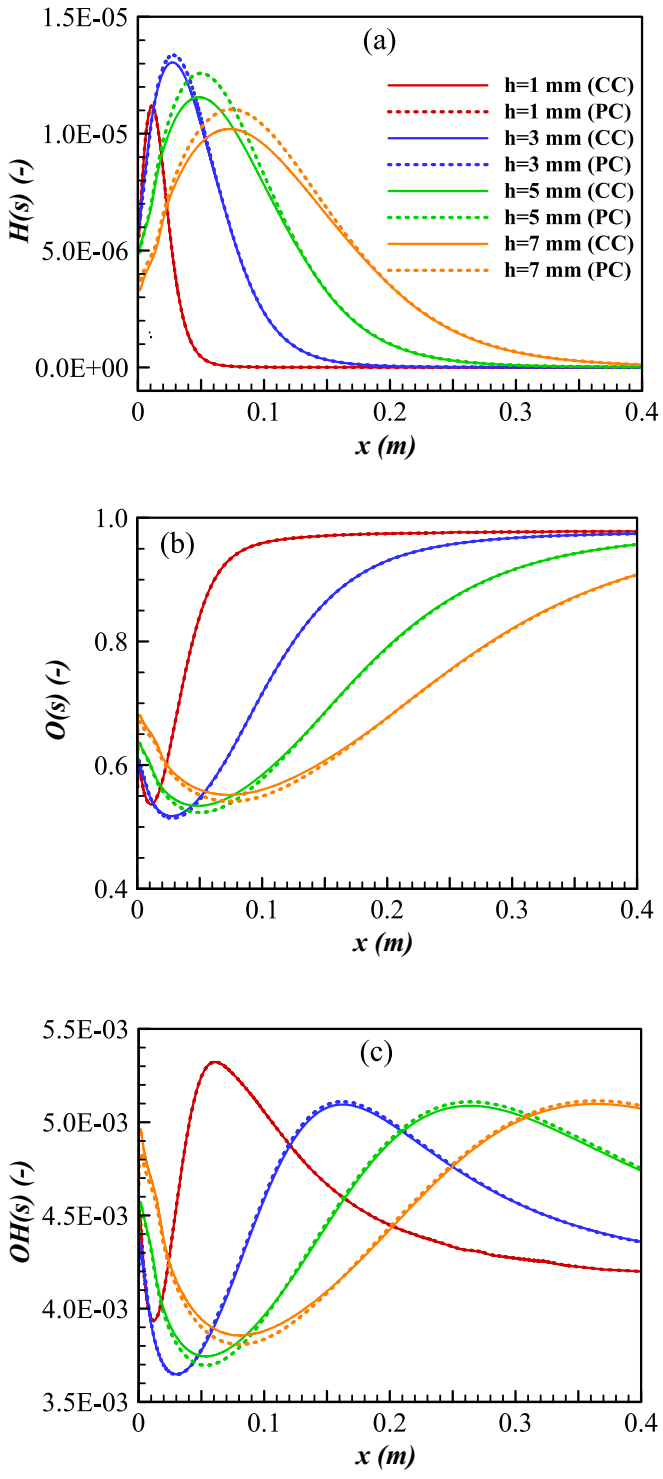

Fig. 6. Surface coverages (a) H(s) (b) O(s) (c) OH(s), φ = 0.15, T_{in} = 300 K, Re = 4200.

Nusselt Number:

$$Nu = \frac{h_c(2h)}{\lambda_g}, \tag{15}$$

where h_c is the heat transfer coefficient and λ_g is the fluid conductivity. The expression for h_c is as follows:

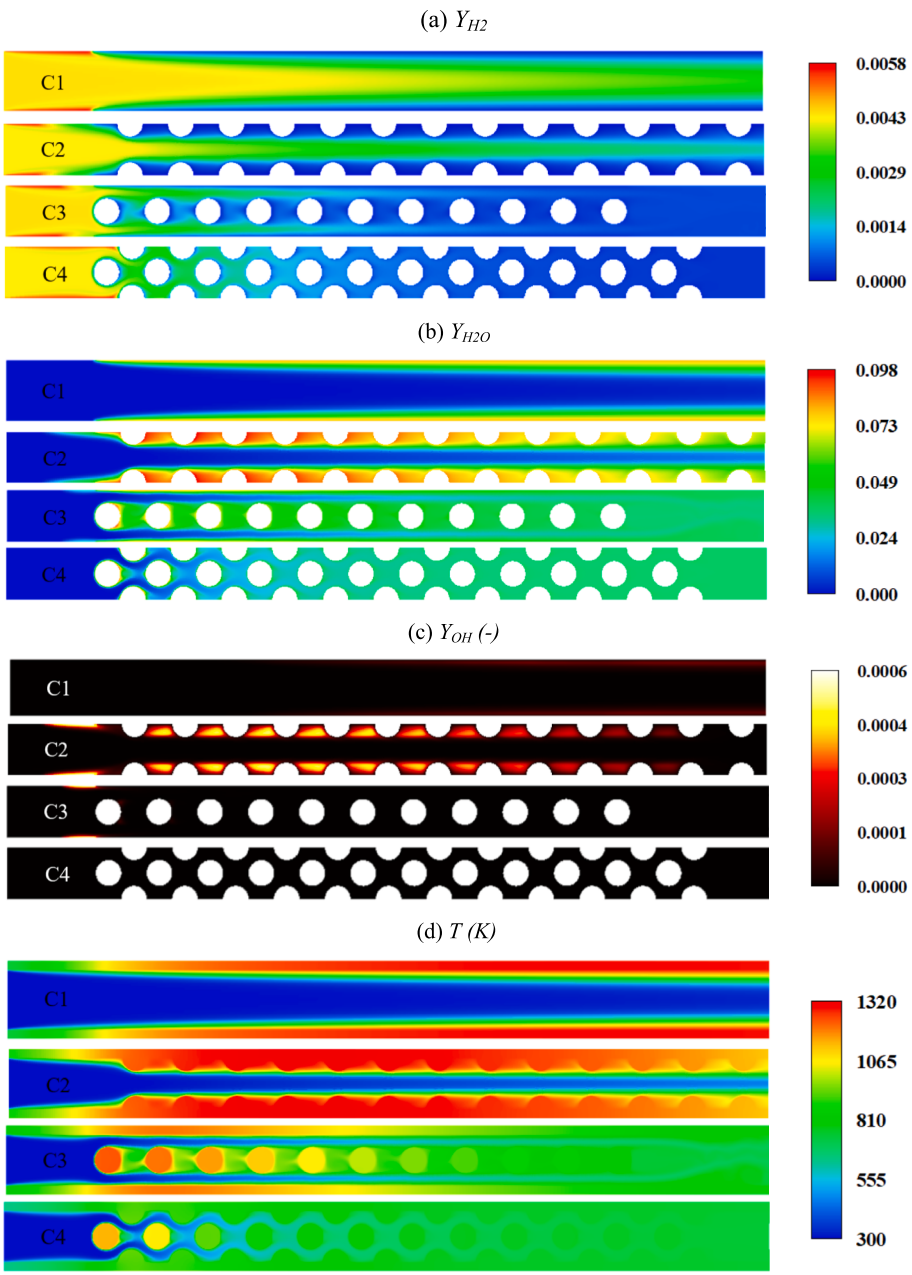

Fig. 7. Contours of (a) Y_{H2} (b) Y_{H2O} (c) Y_{OH} and (d) T for reactors C1, C2, C3 and C4. Reactor length from x = 0 to 57.5-mm is presented, $\varphi = 0.15$, $T_{in} = 300$ K.

$$h_c = \frac{\lambda_g \frac{\partial T}{\partial y}\Big|_w}{T_w - T_{ref}}, \tag{16}$$

where $\partial T/\partial y$ is the gradient of temperature at surface. The T_w and T_{ref} are the surface and the reference temperatures, respectively. For convenience, T_{ref} is considered as an average of T_{in} and T_{adb}.

Sherwood Number:

$$Sh = \frac{k_c(2h)}{D_m}, \tag{17}$$

where k_c and D_m are the H_2 mass transfer coefficient and mass diffusivity, respectively, and k_c is expressed as follows:

$$k_c = \frac{D_m \frac{\partial C_{H2}}{\partial y}\Big|_w}{C_{H2,w} - C_{H2,ref}}, \tag{18}$$

where $\partial C_{H2}/\partial y$ is the gradient of H_2 concentration at surface. $C_{H2,s}$ and $C_{H2,ref}$ are the surface and the reference concentrations of H_2, respectively. $C_{H2,ref}$ is considered as an average of concentrations at T_{in}, and at T_{adb} where H_2 is completely consumed.

Fig. 9 shows the local *Nu* distribution on the catalytic surfaces for different configurations. Here, the *Nu* allows to assess the effectiveness of convective heat transfer processes from hot catalytic surfaces. For configuration C1, the *Nu* is initially high on the catalytic surfaces and gradually decreases along the length of the reactor. However, for configuration C2, a significant variation of *Nu* is observed on the circular surfaces of the half cylinders (HC), and *Nu* is very small on the flat surfaces. There are some locations where *Nu* becomes negative, and this is because of the heat transfer from fluid to solid. Compared to C2, the *Nu* is higher on the surfaces of the full cylinders, and on the flat surfaces in configuration C3. For both cases (C2 and C3), *Nu* on the cylinder surfaces is low at very upstream and downstream of the cylinder and becomes at the maximum upper and lower regimes of the cylinder.

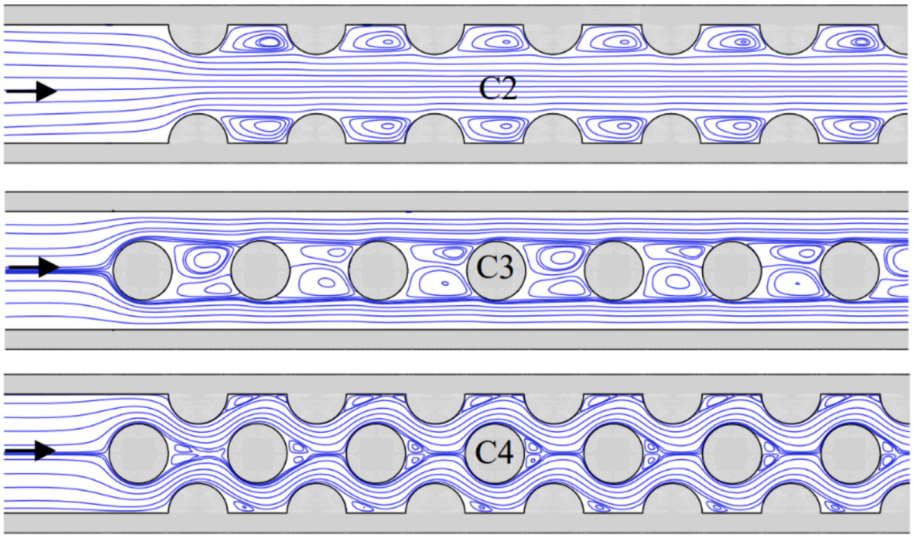

Fig. 8. Streamlines for reactors C2, C3 and C4. Reactor length from x = 2.5-mm to 25.5-mm is presented.

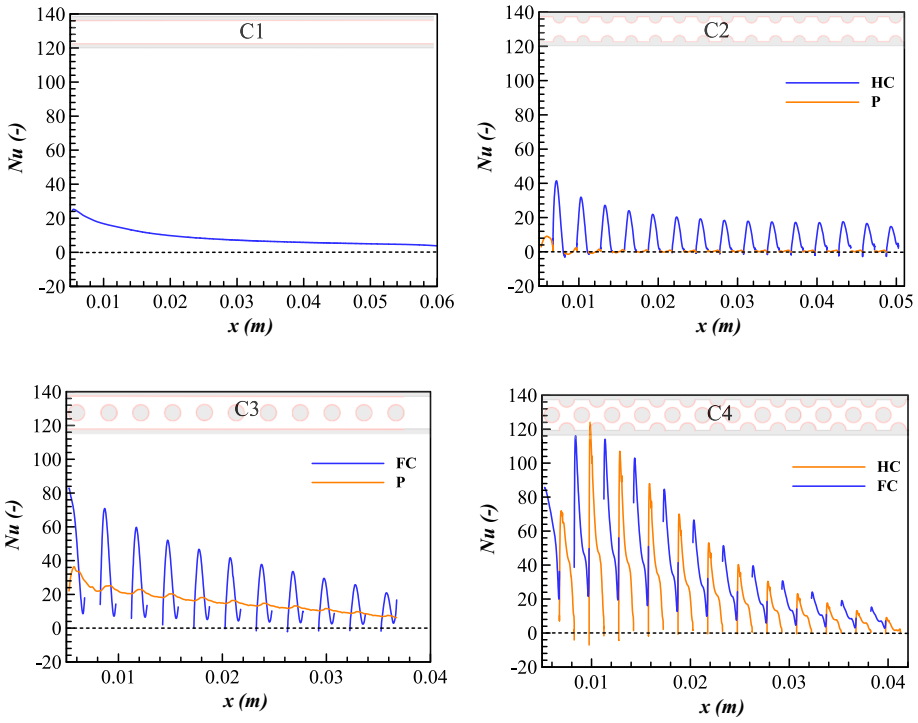

Fig. 9. Nusselt Number (*Nu*) on catalytic surfaces for configurations C1, C2, C3 and C4.

Finally, for C4, *Nu* distributions on the cylinder surfaces are observed to be high and effective among the configurations compared.

Fig. 10 presents the local *Sh* values for the different configurations. Here, the *Sh* measures the effectiveness convective H_2 mass transfer towards the catalytic surfaces. In C1, the *Sh* value sharply decreases at the beginning of the catalytic surfaces due to the high concentration of H_2 clustered near the hot non-catalytic surface. Within a short catalytic length, the *Sh* value drops significantly and remains small with increasing *x*. Comparatively in C2, the variation of *Sh* is observed on circular surfaces, while the contribution on flat surfaces is minimal. This indicates that catalytic process is more effective on circular surfaces than on flat surfaces. Again, the negative *Sh* is the result of a negative gradient of H_2 downstream of the catalytic surfaces. Similarly, in C3, the *Sh* value is higher on circular surfaces except for the downstream portion, and the behaviour on flat surfaces is similar to that of C1. Overall, the *Sh* distributions on the catalytic surfaces of C4 are comparatively higher and effective for higher catalytic activity.

3.2.3. H_2 catalytic conversions

Fig. 11 and Fig. 12 show a comparison of the catalytic performance among the configurations listed in Table 1. The residence time and the amount of catalyst are again kept similar for configurations C1, C2, C3 and C4. The other configurations C5, C6, C7 and C8 are reactors with reduced catalysts, where the catalyst surface area from C4 is decreased for catalyst optimisation. The observations are listed as follows: Fig. 11 (a) presents the H_2 conversion of reactors having the same catalytic surface area. By comparison, the C1 has the lowest performance over the reactor length and achieved a 62.6 % conversion at the end of the

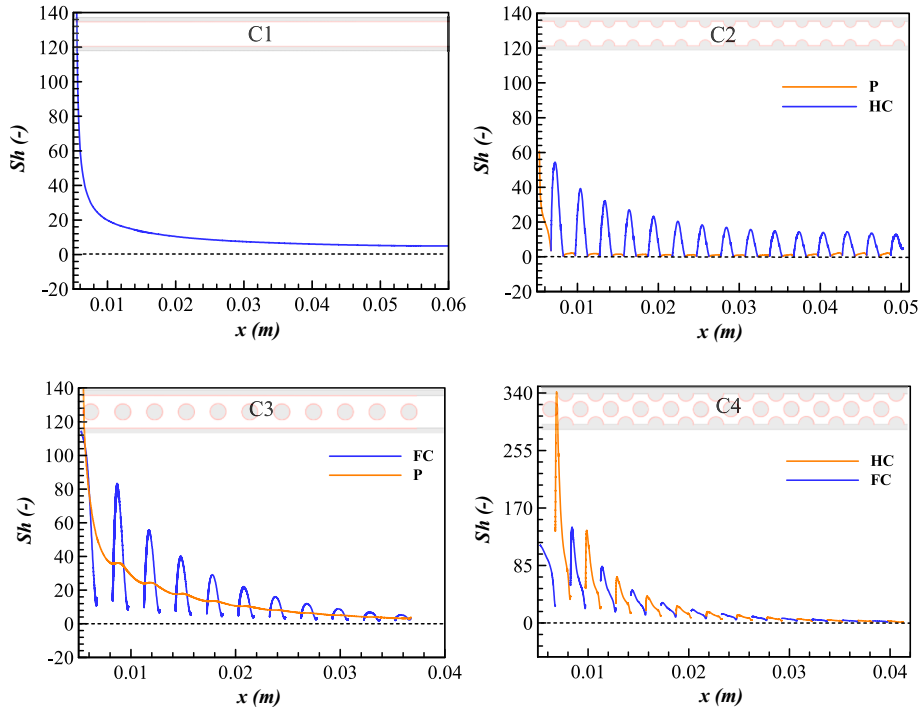

Fig. 10. Sherwood Number (*Sh*) of H_2 on catalytic surfaces for configurations C1, C2, C3 and C4.

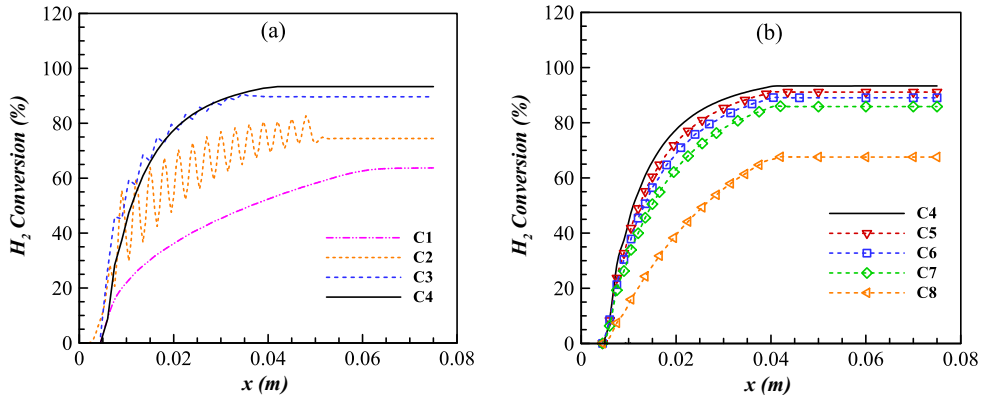

Fig. 11. H_2 Conversion: (a) almost same catalytic surface area, $S_{cat} \approx 0.15$ m^2 (b) Varying S_{cat}.

catalytic region. After that, no conversion occurs because of the absence of the catalyst. For C2, however, the H_2 conversion plot is not as smooth as C1 and has peaks along the reactor length. The peaks and troughs of conversion are attained on the circular and flat surfaces, respectively. The H_2 conversion is effective over the circular surfaces as a result of an increased mass transfer, discussed in Fig. 10. Due to the same reason, there is a high peak value of conversion for C3 in the region between the flat surfaces and cylinders. Comparatively, the mass transfer to the cylinder surfaces of C3 is more effective than C2, therefore, the H_2 conversion values are higher in C3. At the end of catalytic region, the H_2 conversion is achieved by 74.4 % and 89.6 % for C2 and C3, respectively. For C4, the H_2 conversion plot is smooth like C1, and this has the highest possible conversion of 93.3 % at the end of catalytic region. Again, C4 has a lower conversion than C3 over the region of 5.12 mm $< x <$ 21 mm though the mass and heat transfer over that reactor length is effective in C4 as depicted Fig. 9 and Fig. 10. This is because of the relative amount of catalyst coated along the reactor walls which is comparatively high for C3. However, the reactor shape significantly influences the contributions of gaseous and catalytic reaction pathways to H_2 conversion. As shown in Table 4, gaseous conversion in configuration C2 is almost double that of configuration C1, while it is minimal in configuration C3. In configuration C4, the combustion is purely catalytic. Fig. 11(b) shows the H_2 conversion of reactors with varying catalytic surface area. The configuration C4 is chosen for the catalyst optimisation analysis as this has a better heat and mass transfer capability. The additional four configurations C5, C6, C7 and C8 are the same as C4 but have the catalytic surface area of 75 %, 62.5 %, 50 % and 25 %, respectively. The orientation of catalytic surfaces is shown in Fig. 1. However, the catalytic surfaces are selected in those locations where the H_2 mass transfer is relatively high. As expected, the H_2 conversion plots of C5, C6, C7 and C8 are identical with C4 and the conversion values over the reactor length are comparatively low than the immediate reactor of high percentage of catalytic surface. But the catalyst reduction in each reactor configuration is very significant compared to the loss of H_2 conversion. At the end of catalytic region, the H_2 conversion is achieved by 91.08 %, 89.04, 85.83 % and 67.56 % for C5, C6, C7 and C8, respectively. Compared to C4, with a 50 % and 75 % reduction in catalyst, this results in a 7.47 % and 25.74 % reduction in H_2 conversion, respectively. However, the maximum H_2 catalytic conversion rate per unit area is achieved with a 50 % catalyst reduction in

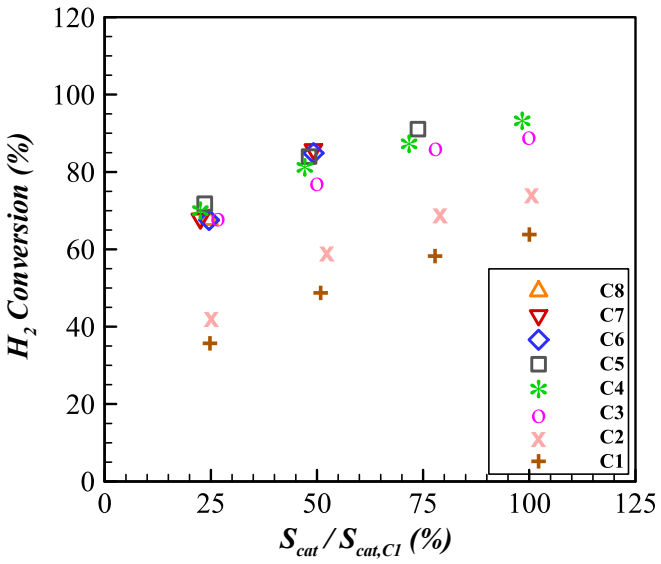

Fig. 12. H_2 conversion as a function of catalyst amount ($S_{cat}/S_{cat,C1}$).

the C7 reactor reported in Table 4.

To assess the reactor performance with a reduced catalyst, Fig. 12 shows the H_2 conversion at different percentages of the catalytic surface area compared to C1 ($S_{cat}/ S_{cat,C1}$). It is noted that the H_2 conversion values are taken keeping the same operating condition as mentioned in Table 1, and estimated at the different axial locations of the reactor, therefore, the residence time at the axial locations is not the same in all the cases. However, the comparison for the catalyst surface area is still useful as the overall residence time in all the reactors are same. As shown in Fig. 12, the H_2 conversions for C1 at different percentages of catalyst are lowest. Comparatively, for C2, there is an improved performance. However, the reactors C3-C8 have similar H_2 conversions which are significantly high compared to C1 and C2. At ~ 25 % catalyst, the H_2 conversion is in the range of 67–71 % for C3-C8. When the catalyst percentage is increased to ~ 50 %, the H_2 conversion increases to 77 % and 81–86 % for C3 and C4-C7, respectively. Again, a further increment to ~ 75 % catalyst results in H_2 conversion of 86–91 % for C3-C6. For ~ 100 % catalyst, the maximum conversion is 89–93 % for C3-C4.

To summarise, the reactors with combined HCs and FCs are proved to be effective for an improved catalytic conversion. With segmented coating on HCs and FCs at a similar amount of catalytic surface, the change in H_2 conversion is within 4–5 %. However, this key finding is crucial for developing a cost-effective catalytic reactor. Finally, the catalytic reactors investigated have significant variation in the pressure drop, as listed in Table 5. The pressure drop here is characterised by the percentage decrease from that of the inlet pressure. The high-pressure drop is a consequence of flow separation and constricted flow. However, in catalytic reactor design, finding an optimal balance between H_2 conversion efficiency and pressure drop is essential, as these factors directly influence reactor throughput, energy efficiency, and operational costs. To achieve this balance, future work could focus on optimising design aspects such as reactor geometry, including cylinder size and positioning, improving flow distribution, and selecting effective catalyst coating strategies.

4. Conclusions

Premixed turbulent combustion of highly lean and ultra-lean hydrogen/air mixtures in a planar/non-planar reactor with platinum coating on inner surfaces was numerically investigated. Computations were carried out in multicomponent species transport model of turbulent solver using Ansys Fluent. Prior to analysis, the model was validated with available experimental results. To intensify the catalytic process, the catalytic surfaces are modified in such way to have increased mass and heat convection. The key findings of this work are:

- The reactor with high S/V ratio has significant impact on catalytic process and could burn H_2 completely within shorter length of the catalytically coated region.
- For non-planar configurations, the combined use of half and full cylinders was shown to significantly enhance mass and heat convection, resulting in an overall superior catalytic performance.
- The surfaces where high mass and heat transfer occurred can be coated optimally. A modified non-planar reactor can increase H_2 conversion by 30.7 % compared to an equivalent planar reactor.
- Discrete coating in a non-planar reactor has been proven as a useful approach for catalyst coating optimisation to save catalyst by 50 % while achieving a catalytic conversion rate of 2 kg/s per unit surface area of the catalytically-coated region.

Future studies will attempt to explore the effect of different types of catalysts on the catalytic combustion process.

Table 5
Pressure drops.

Catalytic reactor	Flow volume (10^{-6} x m^3)	Reynolds number	Dimensionless pressure drop (%)
C1	262.5	4353	31.59
C2	198.49	3680	79.79
C3	205.56	3811	90.26
C4	182.58	3385	98.43
C5	182.58	3385	98.43
C6	182.58	3385	98.40
C7	182.58	3385	98.39
C8	182.58	3385	98.30

Table 4
Gaseous and catalytic conversion rates at different catalytic reactor.

Reactor	C1	C2	C3	C4	C5	C6	C7	C8
$\dot{m}_{H2}$ inlet ($\times 10^4$ kg/s)	1.698	1.436	1.487	1.321	1.321	1.321	1.321	1.321
$\dot{m}_{H2}$ outlet ($\times 10^4$ kg/s)	0.635	0.367	0.154	0.088	0.117	0.145	0.187	0.428
Gas. conv. ($\times 10^4$ kg/s)	0.234	0.379	0.051	1E-5	4E-7	9E-6	2E-5	4E-5
Cat. conv. ($\times 10^4$ kg/s)	0.829	0.689	1.280	1.232	1.203	1.175	1.134	0.892
Cat. conv. per unit area (kg/s)	0.720	0.595	1.115	1.090	1.418	1.663	2.005	1.052
Gas. conv. (%)	13.79	26.41	3.49	0.00	0.00	0.00	0.00	0.00
Cat. conv. (%)	48.80	47.97	86.09	93.31	91.09	89.04	85.84	67.56

CRediT authorship contribution statement

Md Nur Alam Mondal: Writing – original draft, Validation, Software, Investigation, Formal analysis, Conceptualization, Data curation, Methodology, Visualization, Writing – review & editing. **Nader Karimi:** Writing – review & editing, Supervision, Conceptualization. **S. David Jackson:** Writing – review & editing, Supervision. **Manosh C. Paul:** Conceptualization, Funding acquisition, Project administration, Resources, Supervision, Writing – review & editing.

Declaration of competing interest

The authors declare that they have no known competing financial interests or personal relationships that could have appeared to influence the work reported in this paper.

Data availability

Data will be made available on request.

Acknowledgements

The first author is a Commonwealth Scholar (CSC ID: BDCS-2020-54), funded by the UK government. The computational results were obtained using ARCHIE-WeSt High Performance Computer (www.archie-west.ac.uk). N. Karimi acknowledges the financial support provided by EPSRC through grant number EP/X019551/1. We thank Dr. John Mantzaras (Paul Scherrer Institut) for sharing useful experimental and numerical data used for validation in this work.

References

Abe, K., Kondoh, T., Nagano, Y., 1995. A new turbulence model for predicting fluid flow and heat transfer in separating and reattaching flows—II. Thermal field calculations. Int. J. Heat Mass Transf. 38, 1467–1481. https://doi.org/10.1016/0017-9310(94)00252-Q.

Appel, C., Mantzaras, J., Schaeren, R., Bombach, R., Inauen, A., Kaeppeli, B., Hemmerling, B., Stampanoni, A., 2002. An experimental and numerical investigation of homogeneous ignition in catalytically stabilized combustion of hydrogen/air mixtures over platinum. Combust. Flame 128, 340–368. https://doi.org/10.1016/S0010-2180(01)00363-7.

Appel, C., Mantzaras, J., Schaeren, R., Bombach, R., Inauen, A., 2004. Catalytic combustion of hydrogen-air mixtures over platinum: validation of hetero/homogeneous chemical reaction schemes. Clean Air 5, 21–44. https://doi.org/10.1615/interjenercleanenv.v5.i1.20.

Appel, C., Mantzaras, J., Schaeren, R., Bombach, R., Inauen, A., 2005. Turbulent catalytically stabilized combustion of hydrogen/air mixtures in entry channel flows. Combust. Flame 140, 70–92. https://doi.org/10.1016/j.combustflame.2004.10.006.

Arani, B.O., Frouzakis, C.E., Mantzaras, J., Boulouchos, K., 2019. Direct numerical simulations of turbulent catalytic and gas-phase combustion of H_2/air over Pt at practically-relevant Reynolds numbers. Proc. Combust. Inst. 37, 5489–5497. https://doi.org/10.1016/j.proci.2018.05.103.

Chabane, A.M., Truffin, K., Angelberger, C., 2020. Direct numerical simulation of catalytic combustion in a meso-scale channel with non-planar walls. Combust. Flame 222, 85–102. https://doi.org/10.1016/j.combustflame.2020.08.033.

Coltrin, M.E., Kee, R.J., Rupley, F.M., Meeks, E. (1996). SURFACE CHEMKIN-III: A Fortran package for analysing heterogeneous chemical kinetics at a solid-surface - gas-phase interface, Albuquerque, NM, and Livermore, CA (United States), https://doi.org/10.2172/481906.

O. Deutschmann, Schmidt, R., Behrendt, F., Warnat, J. (1996). Numerical modeling of catalytic ignition, Symposium (International) on Combustion 26, 1747–1754. https://doi.org/10.1016/S0082-0784(96)80400-0.

Esfandiary, M., Saedodin, S., Karimi, N., 2023. On the effects of surface waviness upon catalytic steam reforming of methane in micro-structured reactors - a computational study. Int. J. Hydrogen Energy. https://doi.org/10.1016/j.ijhydene.2023.06.086.

Forrest, E.C., Hu, L.-W., Buongiorno, J., McKrell, T.J., 2016. Convective heat transfer in a high aspect ratio minichannel heated on one side. J. Heat Transfer 138. https://doi.org/10.1115/1.4031646.

Fumey, B., Buetler, T., Vogt, U.F., 2018. Ultra-low NOx emissions from catalytic hydrogen combustion. Appl. Energy 213, 334–342. https://doi.org/10.1016/j.apenergy.2018.01.042.

Ghermay, Y., Mantzaras, J., Bombach, R., 2010. Effects of hydrogen preconversion on the homogeneous ignition of fuel-lean $H_2/O_2/N_2/CO_2$ mixtures over platinum at moderate pressures. Combust. Flame 157, 1942–1958. https://doi.org/10.1016/j.combustflame.2010.02.016.

Ghermay, Y., Mantzaras, J., Bombach, R., Boulouchos, K., 2011. Homogeneous combustion of fuel-lean $H_2/O_2/N_2$ mixtures over platinum at elevated pressures and preheats. Combust. Flame 158, 1491–1506. https://doi.org/10.1016/j.combustflame.2010.12.025.

Hunt, G., Karimi, N., Mehdizadeh, A., 2021. Intensification of ultra-lean catalytic combustion of methane in microreactors by boundary layer interruptions – A computational study. Chem. Eng. Sci. 242, 116730 https://doi.org/10.1016/j.ces.2021.116730.

Kee, R.J., Dixon-Lewis, G., Warnatz, J., Coltrin, M.E., Miller, J.A. (1986). A Fortran computer code package for the evaluation of gas-phase, multicomponent transport properties, United States. https://www.osti.gov/biblio/7157265.

Kee, R., Rupley, F., Miller, J. (1989). Chemkin-II: A Fortran chemical kinetics package for the analysis of gas-phase chemical kinetics, Albuquerque, NM, and Livermore, CA (United States). https://doi.org/10.2172/5681118.

Kim, T.J., Yetter, R.A., Dryer, F.L., 1994. New results on moist CO oxidation: high pressure, high temperature experiments and comprehensive kinetic modeling. Sympos. (International) Combust. 25, 759–766. https://doi.org/10.1016/S0082-0784(06)80708-3.

Kuper, W.J., Blaauw, M., van der Berg, F., Graaf, G.H., 1999. Catalytic combustion concept for gas turbines. Catal. Today 47, 377–389. https://doi.org/10.1016/S0920-5861(98)00320-4.

Li, Y.-H., Chen, G.-B., Hsu, H.-W., Chao, Y.-C., 2010. Enhancement of methane combustion in microchannels: effects of catalyst segmentation and cavities. Chem. Eng. J. 160, 715–722. https://doi.org/10.1016/j.cej.2010.03.057.

Li, Y.-H., Chen, G.-B., Wu, F.-H., Cheng, T.-S., Chao, Y.-C., 2012. Effects of catalyst segmentation with cavities on combustion enhancement of blended fuels in a micro channel. Combust. Flame 159, 1644–1651. https://doi.org/10.1016/j.combustflame.2011.11.017.

Li, J., Zhao, Z., Kazakov, A., Dryer, F.L., 2004. An updated comprehensive kinetic model of hydrogen combustion. Int. J. Chem. Kinet. 36, 566–575. https://doi.org/10.1002/kin.20026.

Lu, Q., Gou, J., Wang, Y., Fan, B., Zhang, Y., Wang, Y., Quaye, E.K., Pan, J., 2022. Thermal and chemical analysis on the hetero-/homogeneous combustion characteristics of H_2/air mixture in a micro channel with catalyst segmentation. Fuel 320, 123883. https://doi.org/10.1016/j.fuel.2022.123883.

Mantzaras, J., 2006. Understanding and modeling of thermofluidic processes in catalytic combustion. Catal. Today 117, 394–406. https://doi.org/10.1016/j.cattod.2006.06.047.

Mantzaras, J., 2019. Progress in non-intrusive laser-based measurements of gas-phase thermoscalars and supporting modeling near catalytic interfaces. Prog. Energy Combust. Sci. 70, 169–211. https://doi.org/10.1016/j.pecs.2018.10.005.

Mantzaras, J., Bombach, R., Schaeren, R., 2009. Hetero-/homogeneous combustion of hydrogen/air mixtures over platinum at pressures up to 10bar. Proc. Combust. Inst. 32, 1937–1945. https://doi.org/10.1016/j.proci.2008.06.067.

Mantzaras, J. (2014). Catalytic Combustion of Hydrogen, Challenges, and Opportunities, in: Advances in Chemical Engineering, Academic Press Inc., pp. 97–157. 10.1016/B978-0-12-800422-7.00003-0.

Marinov, N.M., Westbrook, C.K., Pitz, W.J. (1995). Detailed and global chemical kinetics model for hydrogen, in: International Symposium on Transport Properties, San Francisco, CA (United States), , 1995. https://www.osti.gov/servlets/purl/90098.

Merk, H.J., 1959. The macroscopic equations for simultaneous heat and mass transfer in isotropic, continuous and closed systems. Appl. Sci. Res. 8, 73–99. https://doi.org/10.1007/BF00411741.

Michelon, N., Mantzaras, J., Canu, P., 2015. Transient simulation of the combustion of fuel-lean hydrogen/air mixtures in platinum-coated channels. Combust. Theor. Model. 19, 514–548. https://doi.org/10.1080/13647830.2015.1056832.

Mondal, M.N.A., Karimi, N., Jackson, S.D., Paul, M.C., 2023. Numerical investigation of premixed hydrogen/air combustion at lean to ultra-lean conditions and catalytic approach to enhance stability. Int. J. Hydrogen Energy 48, 18100–18115. https://doi.org/10.1016/j.ijhydene.2023.01.298.

Pizza, G., Frouzakis, C.E., Mantzaras, J., Tomboulides, A.G., Boulouchos, K., 2008. Dynamics of premixed hydrogen/air flames in microchannels. Combust. Flame 152, 433–450. https://doi.org/10.1016/j.combustflame.2007.07.013.

Pizza, G., Mantzaras, J., Frouzakis, C.E., Tomboulides, A.G., Boulouchos, K., 2009. Suppression of combustion instabilities of premixed hydrogen/air flames in microchannels using heterogeneous reactions. Proc. Combust. Inst. 32, 3051–3058. https://doi.org/10.1016/j.proci.2008.05.055.

Qazi Zade, A., Renksizbulut, M., Friedman, J., 2012. Contribution of homogeneous reactions to hydrogen oxidation in catalytic microchannels. Combust. Flame 159, 784–792. https://doi.org/10.1016/j.combustflame.2011.07.016.

Schlegel, A., Benz, P., Griffin, T., Weisenstein, W., Bockhorn, H., 1996. Catalytic stabilization of lean premixed combustion: method for improving NOx emissions. Combust. Flame 105, 332–340. https://doi.org/10.1016/0010-2180(95)00211-1.

Schultze, M., Mantzaras, J., 2013. Hetero-/homogeneous combustion of hydrogen/air mixtures over platinum: fuel-lean versus fuel-rich combustion modes. Int. J. Hydrogen Energy 38, 10654–10670. https://doi.org/10.1016/j.ijhydene.2013.06.069.

Smith, L.L., Karim, H., Castaldi, M.J., Etemad, S., Pfefferle, W.C., Khanna, V., Smith, K. O., 2005. Rich-catalytic lean-burn combustion for low-single-digit NOx gas turbines. J. Eng. Gas Turbine Power 127, 27–35. https://doi.org/10.1115/1.1787510.

Stewart, W.E., 1995. Multicomponent mass transfer. By Ross Taylor and R. Krishna, Wiley, New York, 1993, 579 pp. AIChE J. 41, 202–203. https://doi.org/10.1002/aic.690410124.

Sui, R., Mantzaras, J., 2016. Combustion stability and hetero-/homogeneous chemistry interactions for fuel-lean hydrogen/air mixtures in platinum-coated microchannels.

Combust. Flame 173, 370–386. https://doi.org/10.1016/j.combustflame.2016.08.011.

Sui, R., Prasianakis, N.I., Mantzaras, J., Mallya, N., Theile, J., Lagrange, D., Friess, M., 2016. An experimental and numerical investigation of the combustion and heat transfer characteristics of hydrogen-fueled catalytic microreactors. Chem. Eng. Sci. 141, 214–230. https://doi.org/10.1016/j.ces.2015.10.034.

Sui, R., Es-sebbar, E., Mantzaras, J., Prasianakis, N.I., 2018. Experimental and numerical investigation of fuel-lean H_2 /CO/air and H_2/CH_4/air catalytic microreactors. Combust. Sci. Technol. 190, 336–362. https://doi.org/10.1080/00102202.2017.1391231.

Vincent-Randonnier, A., Sabelnikov, V., Ristori, A., Zettervall, N., Fureby, C., 2019. An experimental and computational study of hydrogen–air combustion in the LAPCAT II supersonic combustor. Proc. Combust. Inst. 37, 3703–3711. https://doi.org/10.1016/j.proci.2018.05.127.

Wang, S., Chen, L., Niu, F., Chen, D., Qin, L., Sun, X., Huang, Y., 2016. Catalytic combustion of hydrogen for residential heat supply application. Int. J. Energy Res. 40, 1979–1985. https://doi.org/10.1002/er.3579.

Warnatz, J., Allendorf, M.D., Kee, R.J., Coltrin, M.E., 1994. A model of elementary chemistry and fluid mechanics in the combustion of hydrogen on platinum surfaces. Combust. Flame 96, 393–406. https://doi.org/10.1016/0010-2180(94)90107-4.

Zheng, X., Mantzaras, J., 2014. An analytical and numerical investigation of hetero-/homogeneous combustion with deficient reactants having larger than unity Lewis numbers. Combust. Flame 161, 1911–1922. https://doi.org/10.1016/j.combustflame.2013.12.018.